Article:
Chen, Y.-M., Zang, L.-S., Koc-Bilican, B. et al. (2022) Macroporous surgical mesh from a natural cocoon composite. ACS Sustainable Chemistry & Engineering, 10 (18). pp. 5728-5738. ISSN: 2168-0485

https://doi.org/10.1021/acssuschemeng.1c06941

A macroporous surgical mesh from a natural cocoon composite

Lian-Sheng Zang[a,*], Yong-Ming Chen[a], Behlul Koc-Bilican[b,c], Ismail Bilican[c,d,e], Chris Holland[f], Demet Cansaran-Duman[g], Tugce Karaduman[b], Arzu Colak[h], Yasin Bayır[i], Zekai Halici[j], Sevilay Ozmen[k], Asad Ali[l], Jalel Labidi[m], Caglar Elbuken[e,n], Murat Kaya[b,c,*]

[a] *Key Laboratory of Green Pesticide and Agricultural Bioengineering, Guizhou University, 550025 Guiyang, China*
[b] *Department of Biotechnology, Faculty of Science and Letters, Aksaray University, 68100 Aksaray, Turkey*
[c] *ASUBTAM-Science and Technology Application and Research Center, Aksaray University, 68100 Aksaray, Turkey*
[d] *Department of Electronics and Automation, Technical Vocational School, Aksaray University, 68100 Aksaray, Turkey*
[e] *UNAM—National Nanotechnology Research Center, Institute of Materials Science and Nanotechnology, Bilkent University, 06800 Ankara, Turkey*
[f] *Department of Materials Science and Engineering, University of Sheffield, Mappin Street, Sheffield S1 3JD, United Kingdom*
[g] *Institute of Biotechnology, Ankara University, 06110 Ankara, Turkey*
[h] *Department of Physics, Faculty of Arts and Sciences, Clarkson University, 13699 New York, USA*
[i] *Department of Biochemistry, Faculty of Pharmacy, Ataturk University, 25240 Erzurum, Turkey*
[j] *Department of Medical Pharmacology, Faculty of Medicine, Ataturk University, 25240 Erzurum, Turkey*
[k] *Department of Pathology, Ataturk University Faculty of Medicine, 25240 Erzurum, Turkey*
[l] *Department of Agriculture, Abdul Wali Khan University, Mardan, 23200 Khyber Pakhtunkhwa, Pakistan*
[m] *Biorefinery Processes Research Group, Department of Chemical and Environmental Engineering, University of the Basque Country (UPV/EHU), Plaza Europa 1, 20018 Donostia-San Sebastian, Spain*
[n] *Faculty of Biochemistry and Molecular Medicine, Faculty of Medicine, University of Oulu, 90014 Oulu, Finland*

Corresponding Author

Murat Kaya

* Address: Aksaray University, Faculty of Science and Letters, Department of Biotechnology, 68100, Aksaray, Turkey.
E-Mail: muratkaya3806@yahoo.com
Tel.: +90-382-288-2216

Graphical abstract

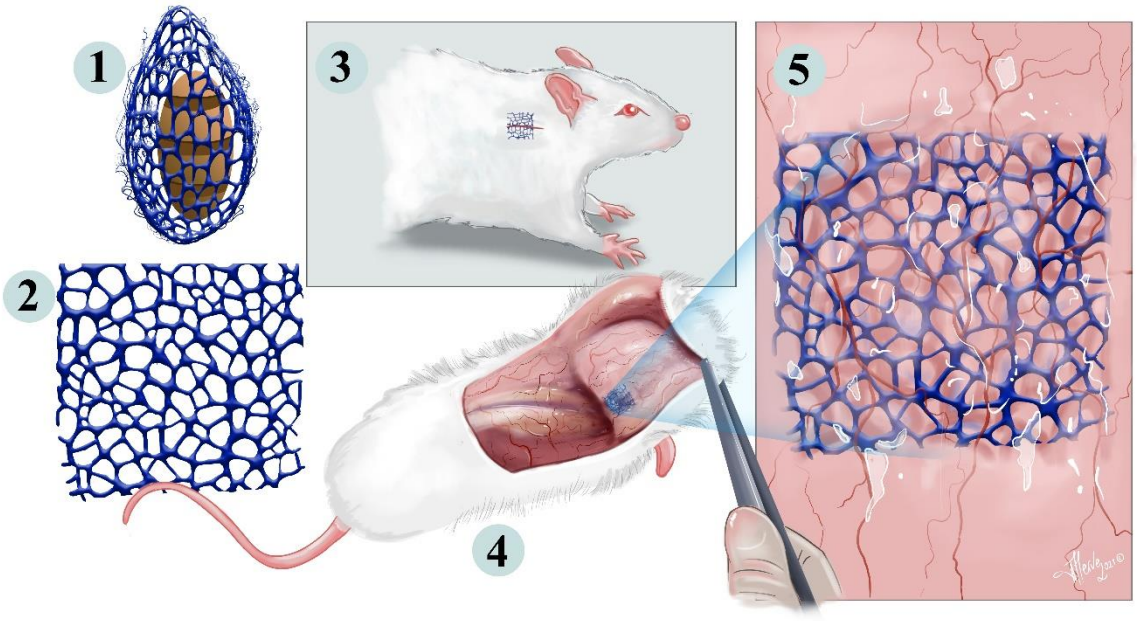

ABSTRACT

Recently, traditional polymer-based surgical meshes have drawn unwanted attention as a result of host tissue complications arising from infection, biocompatibility, and mechanical compatibility. Seeking an alternative solution, we present a hierarchically structured nanofibrous surgical mesh derived from the naturally woven cocoon of the Japanese giant silkworm, termed MothMesh. We report that it displays nontoxicity, biocompatibility, suitable mechanical properties, and porosity while showing no adverse effect in animal trials and even appears to enhance cell proliferation. Hence, we assert that the use of this natural material may provide an effective and improved alternative to existing synthetic meshes.

Keywords: Sustainable material; Fibroin; Sericin; Biocompatibility; Surgical mesh; Tissue engineering

1. INTRODUCTION

Surgical meshes are generally used in skull injuries, tendon repairs, and eye surgeries especially in hernia, pelvic organ prolapses, and urinary incontinence stress.[1-4] Historically, owing to their density and lack of elasticity, metal prostheses used to treat these diseases find it challenging to adapt to soft tissue applications.[5] However plastic-based meshes such as polypropylene and polytetrafluoroethylene have provided major advantages thanks to their flexibility, strength, and lightness, although the biocompatibility issues surrounding plastic meshes have not been completely resolved.[6] Furthermore, the use of non-biocompatible synthetic mesh in certain cases may lead to serious complications such as pain, infection, erosion, inflammation, and restriction of movement. In order to address the adverse effects of synthetic polymer meshes, absorbable meshes consisting of polyglycolic acid, polylactic acid, trimethylene carbonate and poly-4-hydroxybutyrate combinations have been proposed and developed subsequently.[7] While these show similar results after implantation to permanent synthetic meshes, they have relatively short clinical stabilization times after being fully absorbed.[8] While mesh renewal increases the risk of local infection that ultimately leads to infectious disease, it is often necessary to avoid future discomfort. An alternative to metal and synthetic polymer meshes that attempts to address some of the above shortcomings is looking towards the use of biological materials.[9] In the literature, decellularized meshes have been developed from sources such as human, sheep, bovine, or pig that contain extracellular tissue matrix.[10-11] Although biological meshes provide three-dimensional support and scaffolding for tissue-specific cell proliferation, signaling, and cell remodeling, they are not perfect; with cost and mechanical properties often being issues.[12-13] In addition, biological materials are difficult to standardize since they come from various human or animal tissues, a problem further confounded by variations in decellularization and other phases of production.[14]

Hence the search is on to develop a material that meets the requirements of a surgical mesh; sustainability, biocompatibility, matched mechanical properties and a porous structure that enables surgical manipulation and implantation as well as growth and regeneration of host tissue.[15-16] For this purpose, we believe an appropriate solution may be found in bio-based natural mesh materials. Due to its biological origin, history of use, commercial availability and biocompatibility, the silk protein produced by the mulberry silkworm, *Bombyx mori* as it spins cocoon is the most widely used silk in the medical field.[17-18] Silk acquired from these moths consists of two main types of protein; fibroin which forms the fibre and sericin, a gum protein covering the fibre which serves as a matrix material to bind the fibres together in the cocoon.[19]

Typical biomedical applications of silk utilize the protein components in isolation, with sericin was extracted by a degumming process and fibroin then being regenerated back into a liquid prior to reprocessing into a variety of forms.[17, 20-26]

When regenerated, silk fibers have increased potential for use as biomaterials and particularly meshes thanks to their relative ease of processing, controllable degradability, high tensile strength, biocompatibility, soft tissue repair, non-toxicity, low antigenicity and non-inflammatory properties.[27-30] Previous studies have shown that most of the surgical meshes designed using silk fibroin protein have been produced by dissolution in LiBr.[31-33] However, the mechanical properties (strength and flexibility) of regenerated fibroin fibers are usually weakened due to the associated damage caused during an unrefined regeneration process and subsequent loss of the ability for the material to self-assemble into an integrated hierarchical structure.[34-36] Despite considerable effort to overcome these limitations, the mechanical properties are still yet to match the natural fibre counterparts.[19, 30, 36-38]

An alternative approach would be to use the material "as spun" from the animal, with minimal preparation in order to preserve its natural structure and desirable properties. However, the cocoon structure of the widely known silk-producing moths (e.g. *Bombyx mori*, *Antheraea pernyi* and *Samia cynthia*) is not suitable for direct use in mesh-based medical applications because they do not have the desired pore structure.[39-40] However these few species represent a miniscule proportion of lepidopteran silk diversity, and upon review it may be possible to find species that not only spin silk that is biochemically amenable to being a biomaterial, but it's gross morphology, the cocoon, is well suited for specific medical applications.

The Japanese Giant Silkworm, *Caligula japonica* Moore, 1872 (Lepidoptera: Saturniidae) is generally considered as a pest due to its damage to the walnut tree is naturally distributed in East Asia, including Korea, Japan, Russia and particularly in China.[41-42] *C. japonica* produces a long oval-shaped brown net-like cocoon which has undergone very little attention from researchers and its medical mesh applications are completely unexplored. In this work, we develop a mesh material from the *C. japonica* cocoon via a mild chemical process in a single step. We show how this process retains macro, micro and nano scale structures and undertake, i) physicochemical, ii) mechanical, iii) *in vitro* and *in vivo* biocompatibility and toxicity characterization. We show that this material is well suited for surgical mesh applications could be developed into an alternative medical mesh.

2. EXPERIMENTAL SECTIONS

2.1. Materials

The cocoons of *C. japonica* were collected in Kangxian, Gansu province (33° 26′ 33.81″ N, 105° 41′ 52.10″ E) (Figure S1) in June 2019, which is the most important walnut production area in northwestern China and one of the area's most seriously damaged by *C. japonica*. The cocoons were stored in an insect cage with mesh and put it in a room so that they were exposed to similar field conditions (23–29 ℃, 60–85% RH and natural photoperiod) and emerged as field populations did from June to September. The cocoon (50 individuals) of *C. japonica* containing pupae shell were taken from Jilin Agricultural University, Changchun, Jilin, P.R. China. Silk proteins (fibroin and sericin) to be used as the control group were isolated from *Bombyx mori* cocoons. *Bombyx mori* cocoons were commercially purchased from Kozabirlik Bursa, Turkey. All the other chemicals used in the study were obtained from Sigma Aldrich.

2.2. Mesh production

C. japonica cocoons were cut vertically and the pupae shell removed. Cocoons were washed several times with distilled water to remove any dirt and dust on the surface. Cocoons were then treated with 0.2M NaOH for 10 min at 80 ℃ to partially remove sericin and washed with distilled water until reaching a neutral pH. Cocoon pieces of different sizes (~ 2 × 5cm) were cut and opened planarly between glass slides with pressure and squeezed flat for 1 h before use (Figure S2). Thicknesses of MothMesh, commercially available polypropylene mesh and Poly mesh were determined by measurements taken from different parts of the 15 different mesh samples created. A digital micrometer (0.001 mm) (Mitutoyo, Shanghai, China) was used to determine the thickness of the meshes. From the 15 different MothMesh samples including commercially available Polypropylene mesh and Poly mesh, 1 × 1 cm pieces were cut and the average weight per cm^2 was calculated.

2.3. Isolation of the sericin and fibroin protein from the mesh

The isolation of sericin and fibroin proteins from *C. japonica* was performed according to the method previously published with some modification.[43] 10 g of mesh material was cut into as small pieces as possible. It was autoclaved for 30 min at 121 ℃ by adding 20 mL of distilled water for each 1g mesh. The solution consisting of a mixture of sericin and fibroin was filtered with Whatman filter paper. The mesh fibroin was separated by the filtration process. 1: 1 (v/v)

cold methanol was added to the sericin solution and after incubation at + 4 ℃ for 30 min, it was centrifuged at 6000 rpm for 10 min. Sericin pellet and fibroin protein were dried in an oven at 80 ℃. *B. mori* cocoons used as the control group were similarly cut into small pieces and the same isolation steps were applied. Commercially available sericin and fibroin proteins were obtained as pure.

2.4. Characterization

Fourier Transform Infrared spectra (FT-IR) of mesh, mesh sericin and mesh fibroin were obtained using a Perkin Elmer Spectrum Two FT-IR Spectrometer purged with dry air and fitted with a Universal Attenuated Total Reflectance accessory with an internal reflection diamond crystal lens across the wavenumber range of 600-4000 cm^{-1} 8 cm^{-1} resolution, 64 scans. FT-IR spectra of commercial sericin and fibroin were also recorded to interpret functional groups comparatively. The surface morphologies of mesh, mesh sericin and mesh fibroin including commercial sericin and fibroin were revealed by Scanning Electron Microscopy (SEM) on a FEI QUANTA FEG 250 model at 5 kV. The materials were gold-plated using a sputter coater (Cressington sputter-coated 108 Auto, TED PELLA, INC) for 30 sec before the analysis. Energy dispersion spectrum (EDS) was obtained at 20 kV and 5000X magnification (EDAX-Octane Pro). Thermogravimetric analyses (TGA) were performed using a TGA Exstar-TG/DTA 7300 Instruments. The analysis was carried out under a nitrogen atmosphere (3 mL/min purge rate) at a heating rate of 10 ℃/min in the range of 30-900 ℃ using a platinum crucible. Further thermal analysis was measured using a SETARAM DSC131Evo differential scanning calorimeter (Caluire, France). Approximately 5 mg of each sample was placed in a hermetic aluminum pan and tested between 30 and 550 ℃ at a heating rate of 5 ℃/min under an argon gas atmosphere. X-Ray Diffraction (Bruker AXS D8 Advance) analyses of all produced silk protein samples were performed at 40 kV and 30 mA in the scanning angle range of 10-60° at 2θ.

Crystallinity of the MothMesh was calculated according to the following formula;

$$CrI_{110} = [\ (I_{110} - I_{am})\ /\ I_{110}\ ] \times 100 \qquad (1)$$

where, CrI = % crystallinity value, I_{110} = maximum intensity value at 2θ and 20° and I_{am} = maximum intensity value of the amorphous peak at 2θ ,and 13°.

Atomic force microscopy (AFM) has been used for both high-resolution surface topography imaging and nanomechanical properties (i.e., Young's modulus and adhesion force). The measurements were carried out with a CoreAFM (Nanosurf, Switzerland) at ambient conditions using silicon cantilevers (PPP-NCHR, Nanosensors) with a nominal spring constant of 30 N/m. The surface topography images were recorded in tapping mode and processed with the scanning probe microscopy data analysis software package Gwyddion 2.53. To probe adhesion forces and elastic moduli, maps of 10 × 10 force-distance curves were obtained on 5 μm by 5 μm scanned areas at different locations. In total, 644 force-distance curves were recorded with a maximum applied load of 100 nN to ensure the indentation was lower than 10% of sample thickness. Each force-distance curve was processed by correcting baseline offset and tilt of the curves as well as subtracting cantilever bending from the curves with AtomicJ software to convert force-distance curves to force-indentation curves. From indentation curves, the elastic moduli were calculated by fitting the Derjaguin-Muller-Toporov (DMT) model[44] to the approach part of the curves, while the adhesion forces were calculated as the lowest negative rupture force recorded when retracting the probe from the sample surface.

Tensile test of the MothMesh were performed using an Instron 5967 tester (Instron, Norwood, MA, USA). The test was carried out with a cross head speed of 3 mm/min and a load cell was of 500 N. Eight replicates of each sample of 5 × 50 mm were used to obtained the average values of tensile strength, Young´s modulus and elastic modulus.

2.5. Cell culture

L929 mouse fibroblasts (HUKUK, Sap Institute, Ankara, Turkey) were cultured in a humidified incubator with 5% CO_2 at 37 °C using Dulbecco's modified Eagle's medium (DMEM) containing 10% fetal bovine serum (FBS), penicillin (100 U/mL) and streptomycin (100 μg/mL). Cells were monitored daily by using an inverted microscope. Passages were performed twice a week when an 80% of confluence was observed.

2.6. Fluorescence microscope and SEM observation of L929 cells

To further examine the cytocompatibility of the experimental materials, the morphology of L929 cells was observed using a fluorescence microscope (Leica DM3000 (filter cubes: Hoechst 33258, λex: 352 nm, λem: 461 nm; fluorescein diacetate, λex: 490 nm, λem: 526 nm)) and SEM (FEI QUANTA FEG 250). Before analysis, cells grown onto different materials were

washed with phosphate-buffer saline (PBS), fixed with 4% paraformaldehyde for 30 min of two image analysis. For fluorescence imaging, the fixed samples were co-stained with fluorescein diacetate and Hoechst 33258. In addition to SEM observation, experimental materials were dehydrated with a series of increasing gradient ethanol solutions (20, 50, 70, 90 and 100% ethanol), and air-dried. Materials were gold-plated before analysis (Cressington sputter-coated 108 Auto, TED PELLA, INC.).

2.7. Determination of cell proliferation with MTT assay and xCELLigence real-time cell analyzer

Cytotoxicity analysis was assessed by 3-(4,5-dimethylthiazol-2-yl)-2,5-diphenyltetrazolium bromide) (MTT) assay according to the manufacturer´s recommendations (MTT M5655, Sigma ®). Briefly, by adding 2 × 5 mm sterilized MothMesh materials to L929 cells in the logarithmic phase; and then cells were incubated with these materials for 24, 48 and 72 h. Afterward, cell viability measurements were performed compared to the control. The experiments were repeated three times, and data represented as the mean of sixplicate wells ± SEM. The detailed protocol and results of MTT assay has been provided in the Supporting Information.

Cell proliferation analysis was performed with the xCELLigence Real-Time Cell Analysis instrument (RTCA, ACEA Biosciences, Roche, Germany). Cell culture media (100 µl) was added each well in the 16-well e-plate (ACEA Biosciences, RTCA, Roche, Germany) for background measurement. L929 cells were seeded at 1×10^4 cells/well in 16-well e-plate. Cell index (CI) was measured every 15 min for 96 h. After the cells growth period, sterilized test materials (2 × 5 mm size for mesh material, 1 mg for MothMesh, MothMesh sericin, MothMesh fibroin, *B. mori* sericin and fibroin) were added to the 16-well e-plate. The cell index (CI) graph was taken device using the xCELLigence RTCA software program.

2.8. In vivo biocompatibility assay

The local animal ethical committee of Ataturk University approved the study. A total of 14 male adult albino Wistar rats, weighing 250-270 grams were used in this experiment. For the surgical procedure animals were anesthetized with ketamine (100 mg/kg) / ksilasine (10 mg/kg) and the 1×1 cm of the MothMesh material was located in peritoneal cavity of animals. The same protocol was applied and the MothMesh material was implanted subcutaneously

bilaterally below the axilla. Animals were kept under aseptic conditions for the entire duration of the study. After implantation, the rats were located in their standard cages with free access to water and food. 21 days after implantation the rats were anesthetized and implanted MothMesh materials were excised for macroscopic and histopathologic analyses.

2.9. Histopathological analyses

In our study, histopathological examination was performed to determine whether the MothMesh material would cause a tissue reaction. Tissue samples were embedded in paraffin after 24 h of follow-up in 10% formalin and sectioned at a 5µm thickness for hematoxylin and eosin (HE) staining to examine the tissue structure.

3. RESULTS AND DISCUSSION

3.1. Mesh production and its assembly

The mesh production from the cocoon of *C. japonica* and the schematic 3D hierarchy of the mesh are shown in Figure 1. The cocoon sample was subjected to soft NaOH to remove the residual and free proteins on the surface (Figures 1 and 2A). Nano-sized fibroin protein fibers bind to each other with sericin protein to form micro fibers (Figure1, Figure 2B and C). Then, similarly, the micro fibers bind to each other with sericin protein to form macro fibers (Figure 1 and 2B). As a result, a knitted MothMesh is obtained with a pore diameter ranging from 0.9 to 3.1 mm, mass density of 9.6 ± 2.6 $mg.cm^{-2}$, mesh length from 5.1 to 7.3 cm, and the width from 2.5 to 3.6 cm. The thicknesses of the MothMesh, commercially available Polypropylene mesh and Poly mesh were measured as 682 ± 76 µm, 622 ± 70 µm and 547 ± 42 µm, respectively. The average weights per cm^2 was measured as 7.8 ± 3 mg for MothMesh, 12.7 ± 0.7 mg for Polypropylene mesh and 6.7 ± 0.4 mg for Poly mesh. All these measurements demonstrated that the thickness and weight of MothMesh are acceptable when compared to commercial surgical meshes. The isolation experiment revealed that approximately 71% of the MothMesh consists of fibroin fibers (Figure 2C) and 29% of the sericin (gum) protein (Figure 2D). Also, the fibroin fibers and sericin protein obtained from *B. mori* for comparison have been given in Figure 2E and F.

Figure 1. Schematic illustration of the MothMesh production from the cocoons of *Caligula japonica* and natural assembly of the MothMesh at macro, micro and nanoscales. The cocoon was treated with NaOH and the MothMesh material was produced. Both the micro and nanofibers attached to each other with sericin (gumming) protein. The last image is representation of the long macro, micro and nano fibers.

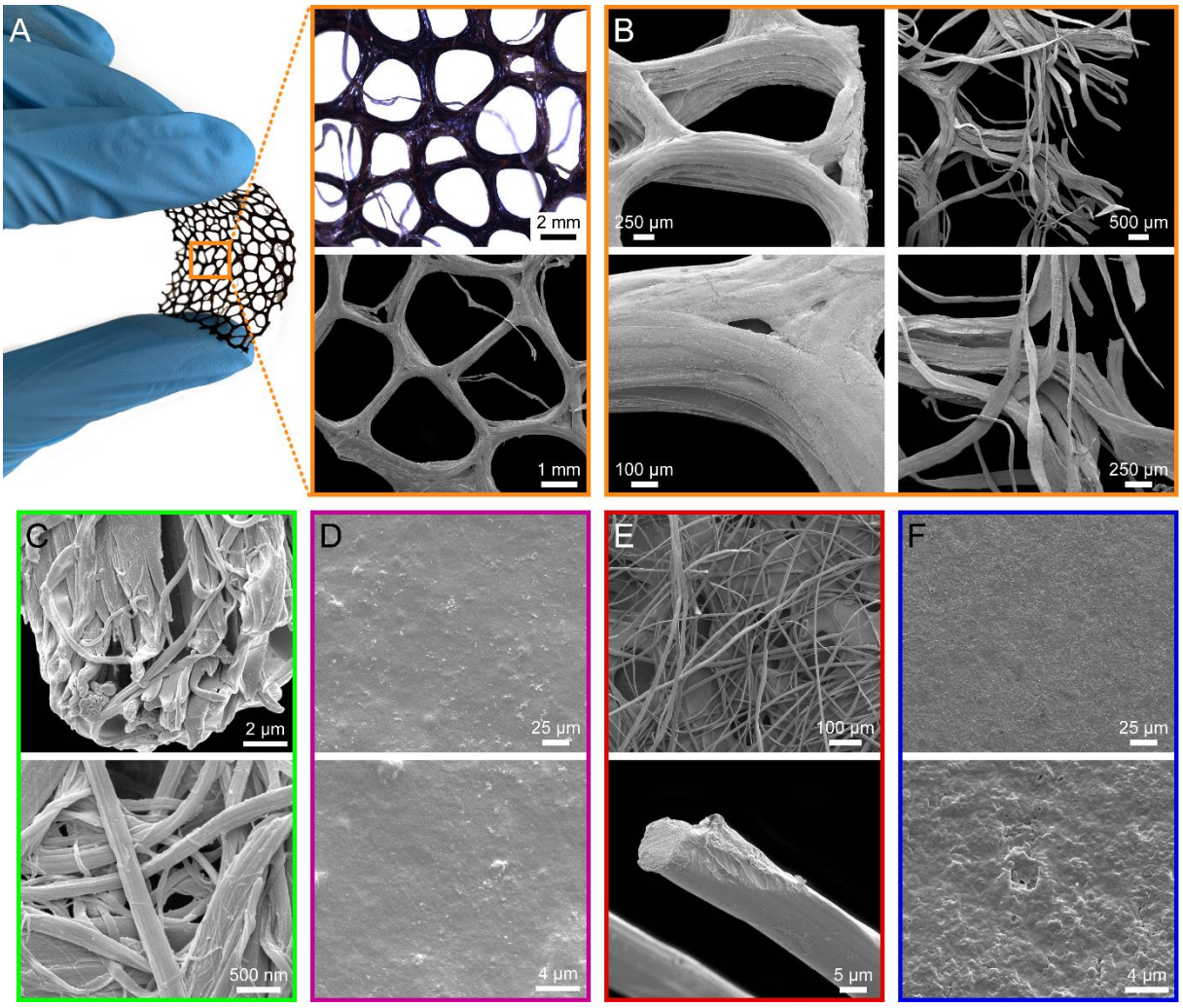

Figure 2. (A) Macro camera, stereo microscope and SEM images showing the flexibility and strength of the MothMesh including surface morphology with porous structure. (B) SEM images representing MothMesh fiber microstructure. Micro fibers are attached to each other with sericin protein and show a strong mechanical property. (C) The SEM images illustrate nano fibers and their attachment to each other by sericin. (D) SEM images of the isolated sericin protein from the MothMesh material. (E) SEM images of commercially known fibroin fibers and (F) sericin isolated from *Bombyx mori*. Additional images for the MothMesh, MothMesh sericin, MothMesh fibroin, *B. mori* sericin and fibroin are provided in the Supporting Information (Figures S3, 4, 5 and 6).

In comparison to the cocoon for *B. mori* there are some clear differences in the structure and appearance of *C. japonica* cocoons. Firstly while the cocoon of *B. mori* is white, the cocoon of *C. japonica* is brownish-yellowish, most likely a result of natural tanning in these "wild" silks.[45-46] The same method was used for the separation of fibroin and sericin proteins from *B. mori* and *C. japonica* cocoons, but it appears the fibroin fibers of *B. mori* become completely separated (Figure 2E), while the fibroin fibers of *C. japonica* were partially separated (Figure 2C), suggesting that the additional crosslinking through tanning provided more strength to the sericin matrix to resist degumming[46], or that the different sericin proteins have different

affinities to fibroin[47] or presence of other compounds may render the NaOH degumming treatment less effective.[48] Sericin samples isolated from *B. mori* and *C. japonica* cocoons and cast into films appear similar, both are consisting of a flat smooth surface (Figure 2D and F).

3.2. Physicochemical characterization

FT-IR spectra of MothMesh and the sericin and fibroin proteins that make it up are shown in Figure 3A. To describe a polypeptide in general, the absorption bands Amide I (1600-1700 cm^{-1}), Amide II (1504-1582 cm^{-1}) and Amide III (1200-1300 cm^{-1}) are characteristic.[49] Amide I band of MothMesh, MothMesh sericin and MothMesh fibroin were recorded as 1627, 1636 and 1623 cm^{-1}, respectively, Amide II band as 1514, 1508 and 1508 cm^{-1}, and Amide III band as 1237, 1230 and 1237 cm^{-1}. Similarly, for commercial sericin purified from *B. mori* used as control and its Amide I, Amide II and Amide III bands are 1626, 1520 and 1241 cm^{-1}, respectively. For commercial fibroin purified from *B. mori*, it was recorded as 1617, 1507 and 1227 cm^{-1}, respectively. The differences recorded in the peaks may be due to changes in the conformation of the protein due to the methanol treatment performed during isolation promoting an increase in β-sheet formation.[50] The large peaks around 3270 cm^{-1} are due to the vibration of O-H groups of intermolecular entrapped water. It was observed that the peaks determined for MothMesh, MothMesh sericin and MothMesh fibroin were comparable with both commercial *B. mori* sericin and fibroin and with the literature.[49] Amide I band observed in the range of 1621-1647 cm^{-1} for proteins is characteristic for the secondary structure antiparallel β-sheet.[49-52] The bands attributed to Amide I (1627, 1636 and 1623 cm^{-1}) for MothMesh, MothMesh sericin, and MothMesh fibroin revealed the presence of antiparallel β-sheet structures. The presence of β-sheet structure in the MothMesh provides the material with superior mechanical properties.[53-54] All the functional groups and vibration modes for each material are given in Table S1.

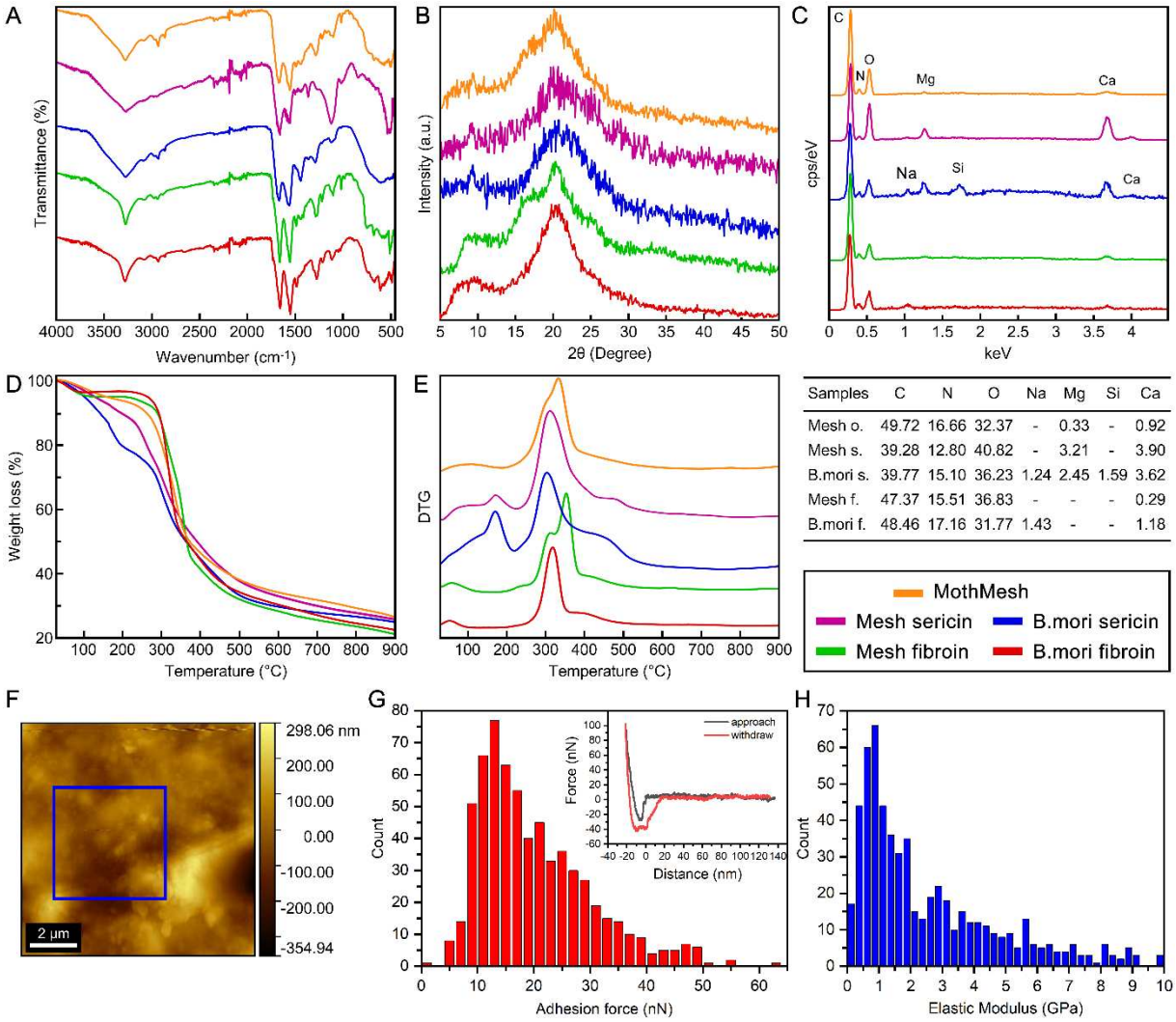

Samples	C	N	O	Na	Mg	Si	Ca
Mesh o.	49.72	16.66	32.37	-	0.33	-	0.92
Mesh s.	39.28	12.80	40.82	-	3.21	-	3.90
B.mori s.	39.77	15.10	36.23	1.24	2.45	1.59	3.62
Mesh f.	47.37	15.51	36.83	-	-	-	0.29
B.mori f.	48.46	17.16	31.77	1.43	-	-	1.18

Figure 3. Characterization of the MothMesh, MothMesh sericin, *Bombyx mori* sericin, MothMesh fibroin and *B. mori* fibroin by (A) FT-IR, (B) XRD, (C) EDS, (D) TGA, (E) DTG, (F) AFM topography image recorded on a MothMesh. The blue box highlights the location of a 5 mm x 5 mm area where the mechanical property measurements were performed. Histograms present the distribution of (G) adhesion forces, and (H) Young's moduli, recorded on three different locations of the mesh surface, respectively. The inset of (G) shows a representative force-distance curve used for the analysis of adhesion forces and Young's moduli.

Crystal structures of MothMesh, MothMesh sericin, MothMesh fibroin and control sericin and fibroin were revealed by XRD measurements. In the literature, silk protein materials are categorized by XRD models and peaks at 11.95, 21.40 and 24.02° correspond to α-helix crystal structure, while those at 9.10, 20.60, 24.60, 29.30 and 30.90° correspond to β-sheet crystal structure.[55-57] According to the XRD analysis, clearly observed peaks were 9.20 and 20.10° for MothMesh, 9.10 and 20.30° for MothMesh sericin, 9.30 and 20.20° for MothMesh fibroin

(Figure 3B). These peaks indicate the presence of β-sheet conformation in the structure. This result also supports the FTIR analysis results. The peaks recorded for MothMesh, MothMesh sericin, and MothMesh fibroin were compatible with *B. mori* sericin (9.20 and 20.60°) and fibroin (9.10 and 20.40°) used as controls (Figure 3B). Crystallinity was calculated as 62% for MothMesh, 63% for MothMesh sericin, 66% for MothMesh fibroin, 63% for *B. mori* sericin and 73% for *B. mori* fibroin.

The elemental compositions and percentages of all the materials were determined by EDS analysis (Figure 3C). The C content of MothMesh was observed to be higher than all other proteins. It was noted that N contents of the MothMesh and fibroin samples were higher than the sericin samples. A slight amount of S was observed in all samples except for mesh fibroin. The S content in sericin samples is also higher than the other samples. Ca was observed in all the samples, but more Ca was recorded especially in sericin samples. While Na was observed in commercial sericin and fibroin samples, it was not observed in sericin and fibroin produced from MothMesh including MothMesh. Additionally, the presence of Mg in both sericin samples was also revealed. It has been observed that the elemental profile recorded for sericin and fibroin produced from MothMesh is compatible with both commercial sericin and fibroin reported in the literature. More data regarding the elemental analysis results are given in Table S2.

TG and DTG curves of the MothMesh, MothMesh sericin, *B. mori* sericin, MothMesh fibroin and *B. mori* fibroin are given in Figure 3D, E and Table S3. The maximum decomposition temperatures of MothMesh, MothMesh sericin, *B. mori* sericin, MothMesh fibroin and *B. mori* fibroin samples were measured as 334 ℃, 304 ℃, 302 ℃, 354 ℃ and 318 ℃, respectively. The sericin samples showed lower thermal stability than the others. Interestingly, MothMesh fibroin has been observed to have higher thermal stability than commercially known fibroin. A remarkable degradation (about 10% of the material mass) occurred at 308 ℃ in the TG/DTG curves of MothMesh fibroin and this can be attributed to tightly bonded sericin to the fibroin fibers. The fibroin samples were obtained by applying the same method to *C. japonica* and *B. mori* cocoons, but TGA analysis clearly demonstrated that *C. japonica* cocoon had more tightly attached fibroin nanofibers with the help of sericin. This result shows that the weave structure and sericin binding of the two cocoons are different.

As a consequence of nanofiber structures of the MothMesh, the surface roughness of the as-prepared MothMesh material was elucidated as 68 nm from high-resolution surface topography

images recorded with AFM (Figure 3F). To investigate the influence of the surface roughness, and sericin protein bonding the fibroin fibers on the adhesion property of MothMesh in nanoscale, force measurements were performed using AFM by recording maps of 10 x 10 force-distance curves (total number, $n = 644$) on 5 μm x 5 μm scanned areas (highlighted blue box of Figure 3F). From the statistical distribution of the measured adhesion forces shown in Figure 3G, the mean adhesion force was found 12 nN. Furthermore, the nanomechanical property of MothMesh was measured using AFM force-distance spectroscopy. The elastic modulus was determined as 1 GPa from the overall histogram composed of all modulus values calculated from maps of force-distance curves (Figure 3H). We hypothesize that the structural alignment of fibroin fibers bonded by sericin proteins could cause such rigid behavior of MothMesh at the nanoscale.

Considering its aligned nanofiber structure, when compared with the nanofiber based commercially available surgical meshes which exhibit a Young's modulus on the scale of tens and hundreds of MPa[16] at the macroscale, the MothMesh has a tensile strength of 8.4 ± 3.5 MPa with 22.2% ± 6.8% elongation and a Young's modulus of 69.1 ± 39.6 MPa at the macroscopic scale (for details see Supportinng Information (Table S4)). Therefore, with its high strength and stretchability competing with commercially available surgical meshes, the MothMesh is a great candidate to be used as a surgical mesh.

3.3. In vitro biocompatibility and cytotoxicity

L929 mouse fibroblast cells attachment onto MothMesh and MothMesh fibroin was observed by fluorescence microscope (Figure 4A,B) and SEM (Figure 4D,E and Figure S7), however, no cell attachment was observed on commercially known fibroin isolated from *B. mori* (Figure 4C, F). The poor cell attachment on commercial fibroin is reported in the literature and numerous modification studies have been conducted to increase cell attachment of commercial fibroin.[58-61] The fibroins dissolved in lithium bromide are used to increase cell attachment in the literature.[62] However, in the present study, cell attachment has taken place on the natural surfaces of MothMesh and MothMesh fibroin samples without any chemical processing (Figure 4A,B,D,E). Here, unlike commercial fibroin, it is thought that the biocompatibility seen in MothMesh and MothMesh fibroin could be due to the composition of the fibroin proteins, potentially harboring cell adhesion motifs, such as RGD sequences, that have been previously observed in "wild" silks.[63-64] Sericin is known to induce proliferation and inhibit apoptosis in mammalian cells and has no adverse effects on the organism.[65-66] In the present study, the

cytotoxic effect of MothMesh, MothMesh sericin, MothMesh fibroin, commercial sericin and fibroin was monitored by MTT assay and real-time xCELLigence system (Figure 4G and Figure S8). MTT analysis showed that no cytotoxicity was observed in cells incubated with MothMesh for 24, 48 and 72 h. (Figure S8). According to xCELLigence system analysis results, it has been observed that MothMesh, MothMesh fibroin and MothMesh sericin have higher cell proliferation enhancing properties than *B. mori* fibroin and sericin (Figure 4G). Accordingly, MothMesh sericin shows the highest proliferative effect, followed by MothMesh and mesh-derived fibroin. Although *B. mori* sericin and fibroin had a proliferative effect on the L929 cell line, proliferative activity of MothMesh, mesh fibroin and mesh sericin was found to be higher.

Wound healing in surgical repairs is a complex and dynamic process involving a series of steps such as hemostasis, inflammation, proliferation and remodeling.[67] Although there are many synthetic mesh materials available commercially, repairs performed with these meshes have several disadvantages, such as inadequate mechanical strength, non-absorbability, chronic inflammatory response and rigid structures that cause bio-incompatibilities, many of which are related to the physicochemical nature of the mesh.[68-70] Improving biocompatibility is critical for a mesh to have better integration into the body and a minimal inflammatory response.[16, 71] To overcome this problem, biological meshes originating from mammalian (e.g. human, sheep, bovine or porcine) source tissues have been produced that reveal a robust and functional extracellular tissue matrix (ECM) that is free of cellular components; however, these materials present difficulties in terms of cost and standardization.[69, 72] In this study, for the first time, a high-strength, flexible and highly biocompatible fibroin and sericin heterocomplex mesh was developed from the natural silk cocoon of *C. japonica*, a cost-effective and natural material produced for centuries with a unique design and precision, with the same standard.

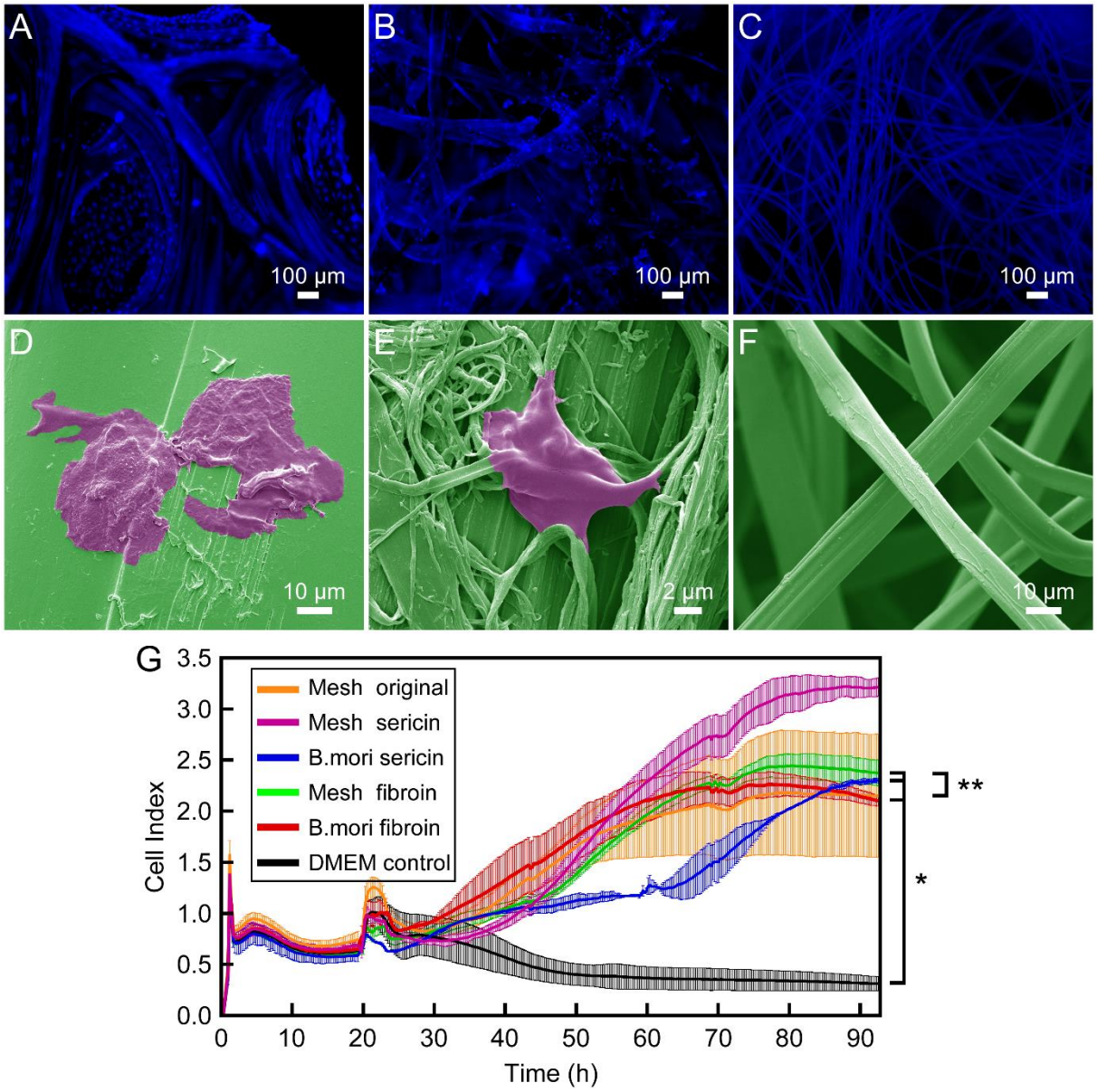

Figure 4. Imaging of cell growth on different biomaterials and cell proliferation results obtained by xCELLigence RTCA system. The L929 cells growing on the mesh material (A) mesh fibroin, (B) commercial fibroin, (C) after 72 h of culture were stained with DAPI for nuclei (blue). SEM images of the three biomaterials seeded with L929 cells and cultured for 72 h (D) Cells-mesh fibroin, (E) Cells-mesh fibroin, (F) Cells-commercial fibroin. (G) The cytotoxic effect of different groups treated with materials for 96 h. *,** denotes statistically significant differences ($n = 3$ per group, $p < 0.05$, $p < 0.01$; respectively).

Silk fibroin has been seen as an exceptional material in wound healing due to its abundance, biodegradability, biocompatibility, mechanical strength, signal molecule stabilization ability, high water and oxygen uptake, and low immunogenicity, and numerous studies of *B. mori*

origin have been conducted.[73-75] On the other hand, it exhibits strong hydrophilic properties thanks to the abundance of hydroxyl, carboxyl and amino functional groups in sericin so that it both maintains the humidity of the environment and helps absorb excess leakage fluids from wounds. This allows it to be a promising wound dressing material for both cosmetic and pharmaceutical applications. Various formulations such as sericin-based films, membranes, hydrogels, porous scaffolds and creams have been reported in the literature.[76] It has also been shown that skin excision wounds treated with sericin cream in the dorsal area of rats healed faster with lower levels of inflammatory response compared to control.[77]

As a result, we have shown that the MothMesh material can promote cell adhesion and proliferation thanks to the biochemical effect of the fibroin and sericin components in its structure. This situation indicates that the material has biocompatibility, which may contribute to minimizing the inflammatory response from the body.

3.4. In vivo biocompability of MothMesh

A foreign body reaction occurs against an exogenous substance that is not specific to the body.[78] Therefore, it is known that when a manufactured surgical material is transferred into the body, polymorphonuclear leukocyte, macrophage and fibroblast infiltration, chronic inflammatory reaction and fibrous tissue formation occur as a foreign body reaction up to approximately four weeks post-implantation as a response at the histological level.[79-80] In our study, necrosis, fibrosis, foreign body reaction and chronic inflammation cells were not detected in the histopathological examination of mouse tissue samples following 2 and 3 weeks of MothMesh implantation (Figure 5). Also, the mouse body tissue accepted the implanted MothMesh material as its own tissue and primary tissue healing was observed in that area. Accordingly, no scar formation was observed. When a surgical mesh is implanted and does not have the proper biocompatibility (either due to the material from which it is made or its structural design), the body responds by encapsulating the foreign system, resulting in a hard scar formation that results in poor tissue assembly.[16, 71] It is known that bio-incompatibility of the material causes rejection of implantation due to scar tissue developed by the immunological system. Considering all the biocompatible properties, the MothMesh will overcome all these undesirable features of the commercial meshes.

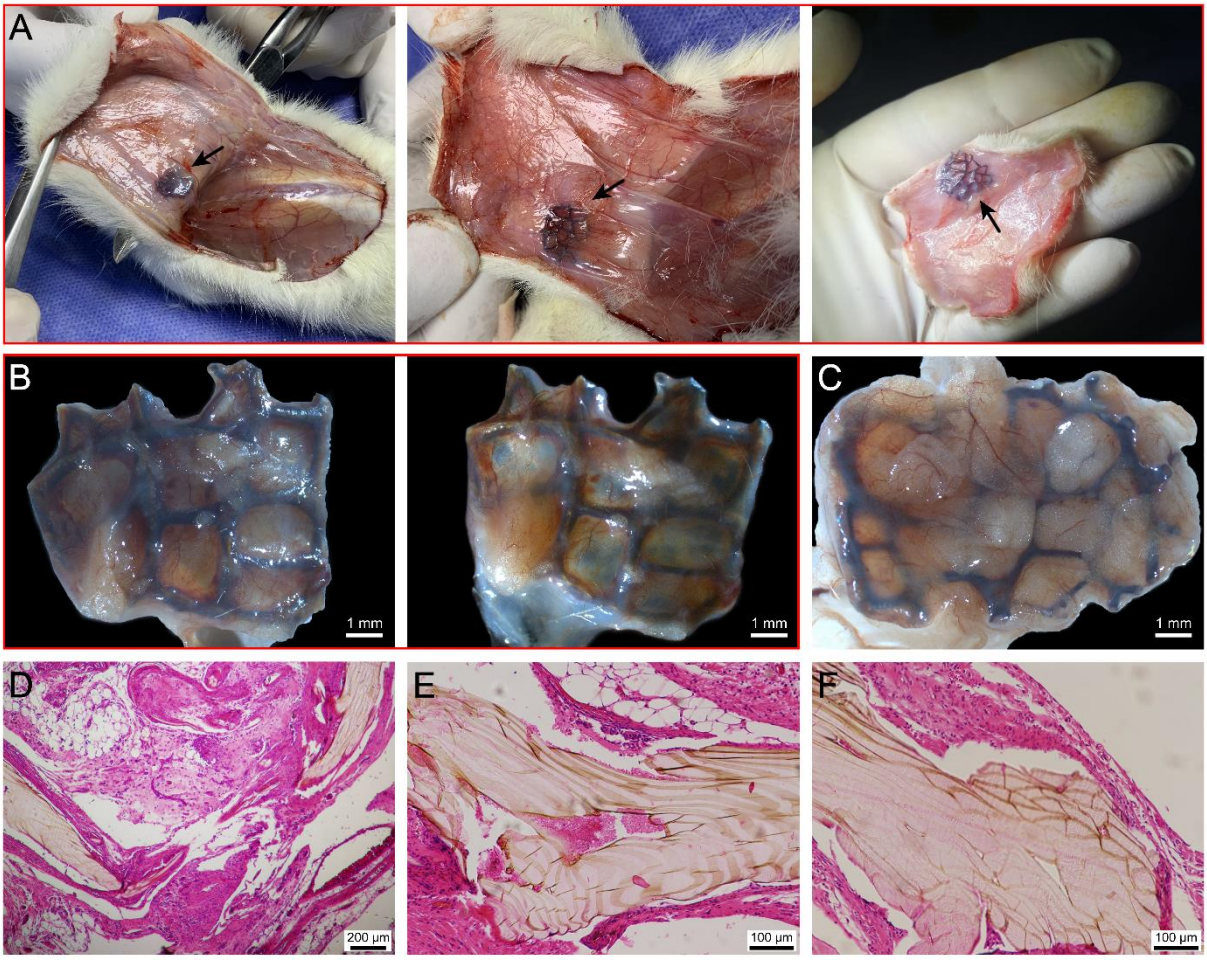

Figure 5. Macroscopical and microscopical view of MothMesh after 21 days of implantation. (A) Appearance during dissection (no inflammation or granulation tissue), (B) and (C) macro appearance after dissection (neovascularisation between mesh squares available) under stereo microscopy, (D), (E) and (F) microscopic appearance after hematoxylin-eosin staining (limited amount of inflammatory cells and evident neovascularisation). More images of MothMesh implanted in the mouse are given in the Figure S9. At the end of 21 days of implantation, it was observed that the shape of MothMesh taken from the mouse was not deformed (Figure S10).

4. CONCLUSION

In summary, a sustainable surgical mesh was produced from the cocoon structure of the *C. japonica* moth. The moth can be cultured easily under laboratory conditions and the processed cocoon it spins has been introduced as a new material; "MothMesh". Through our analysis we have probed its hierarchical structure and self-assembly, revealing that MothMesh has all the properties such as lightness, flexibility, strength and porosity, which place it in good stead to be developed into a surgical mesh. Furthermore our *in-vitro* and *in-vivo* tests confirm the exceptional biocompability of MothMesh allowing it to address the crucial challenge facing

industry. Hence we believe that our approach of conducting a detailed analysis and understanding of the biodiversity of natural material structure and performance will hopefully enable a plethora of novel applications to be discovered. Specifically in this case, the silk of *C. japonica* may have further applications beyond surgical meshes, such as sensing, drug delivery, implant technology and smart textiles.

NOTE

The authors declare no competing financial interests.

ACKNOWLEDGMENTS

This study was funded by Program of Introducing Talents to Chinese Universities (111 Program, D20023). Thanks to ASUBTAM (Aksaray University) for providing laboratory facilities and access to equipment.

REFERENCES

(1) Mirjavan, M.; Asayesh, A.; Jeddi, A. A. A. The effect of fabric structure on the mechanical properties of warp knitted surgical mesh for hernia repair. *Journal of the mechanical behavior of biomedical materials* **2017,** *66*, 77-86.

(2) Taylor, D. The failure of polypropylene surgical mesh in vivo. *Journal of the mechanical behavior of biomedical materials* **2018,** *88*, 370-376.

(3) Wallace, S. J.; Mioton, L. M.; Havey, R. M.; Muriuki, M. G.; Ko, J. H. Biomechanical properties of a novel mesh suture in a cadaveric flexor tendon repair model. *The Journal of hand surgery* **2019,** *44* (3), 208-215.

(4) Chang, Y.; Sun, X.; Li, Q.; Ding, X.; Liu, H.; Wang, J. Silk fibroin scaffold as a potential choice for female pelvic reconstruction: a study on the biocompatibility in abdominal wall, pelvic, and vagina. *Microscopy research and technique* **2017,** *80* (3), 291-297.

(5) DeBord, J. R. The historical development of prosthetics in hernia surgery. *Surgical Clinics of North America* **1998,** *78* (6), 973-1006.

(6) Mangir, N.; Roman, S.; Chapple, C. R.; MacNeil, S. Complications related to use of mesh implants in surgical treatment of stress urinary incontinence and pelvic organ prolapse: infection or inflammation? *World Journal of Urology* **2020,** *38* (1), 73-80.

(7) Wise, J., Surgical mesh for stress urinary incontinence to be halted immediately in England. British Medical Journal Publishing Group: 2018.

(8) Garvey, P. B.; Giordano, S. A.; Baumann, D. P.; Liu, J.; Butler, C. E. Long-term outcomes after abdominal wall reconstruction with acellular dermal matrix. *Journal of the American College of Surgeons* **2017,** *224* (3), 341-350.

(9) Overbeck, N.; Nagvajara, G.; Ferzoco, S.; May, B.; Beierschmitt, A.; Qi, S. In-vivo evaluation of a reinforced ovine biologic: a comparative study to available hernia mesh repair materials. *Hernia* **2020**, 1-14.

(10) Hynes, R.; Naba, A., Overview of the matrisome—an inventory of extracellular matrix constituents and functions. Cold Spring Harb Perspect Biol 4: a004903. 2012.

(11) Brown, B. N.; Badylak, S. F. Extracellular matrix as an inductive scaffold for functional tissue reconstruction. *Translational Research* **2014,** *163* (4), 268-285.

(12) Butler, C. E.; Prieto, V. G. Reduction of adhesions with composite AlloDerm/polypropylene mesh implants for abdominal wall reconstruction. *Plastic and Reconstructive Surgery* **2004,** *114* (2), 464-473.

(13) FitzGerald, J. F.; Kumar, A. S. Biologic versus synthetic mesh reinforcement: what are the pros and cons? *Clinics in Colon and Rectal Surgery* **2014,** *27* (4), 140.

(14) Annor, A. H.; Tang, M. E.; Pui, C. L.; Ebersole, G. C.; Frisella, M. M.; Matthews, B. D.; Deeken, C. R. Effect of enzymatic degradation on the mechanical properties of biological scaffold materials. *Surgical endoscopy* **2012,** *26* (10), 2767-2778.

(15) Orenstein, S. B.; Saberski, E. R.; Kreutzer, D. L.; Novitsky, Y. W. Comparative analysis of histopathologic effects of synthetic meshes based on material, weight, and pore size in mice. *Journal of Surgical Research* **2012,** *176* (2), 423-429.

(16) Baylón, K.; Rodríguez-Camarillo, P.; Elías-Zúñiga, A.; Díaz-Elizondo, J. A.; Gilkerson, R.; Lozano, K. Past, present and future of surgical meshes: a review. *Membranes* **2017,** *7* (3), 47.

(17) Holland, C.; Numata, K.; Rnjak‐Kovacina, J.; Seib, F. P. The biomedical use of silk: past, present, future. *Advanced healthcare materials* **2019,** *8* (1), 1800465.

(18) Kundu, B.; Rajkhowa, R.; Kundu, S. C.; Wang, X. Silk fibroin biomaterials for tissue regenerations. *Advanced drug delivery reviews* **2013,** *65* (4), 457-470.

(19) Li, G.; Li, Y.; Chen, G.; He, J.; Han, Y.; Wang, X.; Kaplan, D. L. Silk‐based biomaterials in biomedical textiles and fiber‐based implants. *Advanced healthcare materials* **2015,** *4* (8), 1134-1151.

(20) Stefan, N.; Miroiu, F. M.; Socol, G. Degradable silk fibroin–Poly (sebacic acid) diacetoxy terminated,(SF-PSADT) polymeric composite coatings for biodegradable medical applications deposited by laser technology. *Progress in Organic Coatings* **2019,** *134*, 11-21.

(21) Kim, D. W.; Lee, O. J.; Kim, S.-W.; Ki, C. S.; Chao, J. R.; Yoo, H.; Yoon, S.-i.; Lee, J. E.; Park, Y. R.; Kweon, H. Novel fabrication of fluorescent silk utilized in biotechnological and medical applications. *Biomaterials* **2015,** *70*, 48-56.

(22) Murugesh Babu, K.; Sahana, N.; Anitha, D.; Kavya, B. Silk fibroin coated antimicrobial textile medical products. *The Journal of The Textile Institute* **2020**, 1-9.

(23) Kim, S. H.; Lee, Y. J.; Chao, J. R.; Sultan, M. T.; Lee, H. J.; Lee, J. M.; Lee, J. S.; Lee, O. J.; Hong, H.; Lee, H. Rapidly photocurable silk fibroin sealant for clinical applications. *NPG Asia Materials* **2020,** *12* (1), 1-16.

(24) Arango, M. C.; Montoya, Y.; Peresin, M. S.; Bustamante, J.; Álvarez-López, C. Silk sericin as a biomaterial for tissue engineering: a review. *International Journal of Polymeric Materials and Polymeric Biomaterials* **2020**, 1-15.

(25) Rockwood, D. N.; Preda, R. C.; Yücel, T.; Wang, X.; Lovett, M. L.; Kaplan, D. L. Materials fabrication from Bombyx mori silk fibroin. *Nature protocols* **2011,** *6* (10), 1612.

(26) Seib, F. P. Emerging silk material trends: repurposing, phase separation and solution-based designs. *Materials* **2021,** *14* (5), 1160.

(27) Cao, Y.; Wang, B. Biodegradation of silk biomaterials. *International journal of molecular sciences* **2009,** *10* (4), 1514-1524.

(28) Guo, C.; Li, C.; Kaplan, D. L. Enzymatic Degradation of Bombyx mori silk materials: a review. *Biomacromolecules* **2020,** *21* (5), 1678-1686.

(29) Guo, C.; Li, C.; Mu, X.; Kaplan, D. L. Engineering silk materials: From natural spinning to artificial processing. *Applied Physics Reviews* **2020,** *7* (1), 011313.

(30) Koeppel, A.; Holland, C. Progress and trends in artificial silk spinning: a systematic review. *ACS Biomaterials Science & Engineering* **2017,** *3* (3), 226-237.

(31) Keirouz, A.; Zakharova, M.; Kwon, J.; Robert, C.; Koutsos, V.; Callanan, A.; Chen, X.; Fortunato, G.; Radacsi, N. High-throughput production of silk fibroin-based electrospun fibers as biomaterial for skin tissue engineering applications. *Materials Science and Engineering: C* **2020**, 110939.

(32) Piluso, S.; Gomez, D. F.; Dokter, I.; Texeira, L. M.; Li, Y.; Leijten, J.; Van Weeren, R.; Vermonden, T.; Karperien, M.; Malda, J. Rapid and cytocompatible cell-laden silk hydrogel formation via riboflavin-mediated crosslinking. *Journal of Materials Chemistry B* **2020,** *8* (41), 9566-9575.

(33) Nikam, V. S.; Punde, D. S.; Bhandari, R. S. Silk fibroin nanofibers enhance cell adhesion of blood-derived fibroblast-like cells: A potential application for wound healing. *Indian Journal of Pharmacology* **2020,** *52* (4), 306.

(34) Boulet-Audet, M.; Holland, C.; Gheysens, T.; Vollrath, F. Dry-spun silk produces native-like fibroin solutions. *Biomacromolecules* **2016,** *17* (10), 3198-3204.

(35) Holland, C.; Terry, A.; Porter, D.; Vollrath, F. Natural and unnatural silks. *Polymer* **2007,** *48* (12), 3388-3392.

(36) Partlow, B. P.; Tabatabai, A. P.; Leisk, G. G.; Cebe, P.; Blair, D. L.; Kaplan, D. L. Silk fibroin degradation related to rheological and mechanical properties. *Macromolecular bioscience* **2016,** *16* (5), 666-675.

(37) Lo, T. J.-c.; Leisk, G. G.; Partlow, B.; Omenetto, F.; Kaplan, D. L.; Kluge, J. A.; Kluge, M. A., High molecular weight silk fibroin and uses thereof. Google Patents: 2015.

(38) Umuhoza, D.; Yang, F.; Long, D.; Hao, Z.; Dai, J.; Zhao, A. Strategies for tuning the biodegradation of silk fibroin-based materials for tissue engineering applications. *ACS Biomaterials Science & Engineering* **2020,** *6* (3), 1290-1310.

(39) Chen, F.; Porter, D.; Vollrath, F. Morphology and structure of silkworm cocoons. *Materials Science and Engineering: C* **2012,** *32* (4), 772-778.

(40) Chen, F.; Porter, D.; Vollrath, F. Silk cocoon (Bombyx mori): multi-layer structure and mechanical properties. *Acta Biomaterialia* **2012,** *8* (7), 2620-2627.

(41) Chen, Y.-M.; Qu, X.-R.; Li, T.-H.; Iqbal, A.; Wang, X.; Ren, Z.-Y.; Desneux, N.; Zang, L.-S. Performances of six eupelmid egg parasitoids from China on Japanese giant silkworm Caligula japonica with different host age regimes. *Journal of Pest Science* **2020**, 1-11.

(42) Chen, Y.-M.; Sun, J.-W.; Iqbal, A.; Lv, R.; Wang, H.; Zang, L.-S. An investigation of Caligula japonica (Lepidoptera: Saturniidae) egg distribution and associated parasitoids on walnut trees (Juglans regia L.) in northwestern China. *International Journal of Pest Management* **2020**, 1-8.

(43) Chirila, T. V.; Suzuki, S.; McKirdy, N. C. Further development of silk sericin as a biomaterial: comparative investigation of the procedures for its isolation from Bombyx mori silk cocoons. *Progress in biomaterials* **2016,** *5* (2), 135-145.

(44) Derjaguin, B. V.; Muller, V. M.; Toporov, Y. P. Effect of contact deformations on the adhesion of particles. *Journal of Colloid and interface science* **1975,** *53* (2), 314-326.

(45) Brunet, P.; Coles, B. C. Tanned silks. *Proceedings of the Royal Society of London. Series B. Biological Sciences* **1974,** *187* (1087), 133-170.

(46) Offord, C.; Vollrath, F.; Holland, C. Environmental effects on the construction and physical properties of Bombyx mori cocoons. *Journal of Materials Science* **2016,** *51* (24), 10863-10872.

(47) Du, S.; Zhang, J.; Zhou, W. T.; Li, Q. X.; Greene, G. W.; Zhu, H. J.; Li, J. L.; Wang, X. G. Interactions between fibroin and sericin proteins from Antheraea pernyi and Bombyx mori silk fibers. *Journal of colloid and interface science* **2016,** *478*, 316-323.

(48) Gheysens, T.; Collins, A.; Raina, S.; Vollrath, F.; Knight, D. P. Demineralization enables reeling of wild silkmoth cocoons. *Biomacromolecules* **2011,** *12* (6), 2257-2266.

(49) Martínez, D. C. C.; Zuluaga, C. L.; Restrepo-Osorio, A.; Álvarez-López, C. Characterization of sericin obtained from cocoons and silk yarns. *Procedia engineering* **2017,** *200*, 377-383.

(50) Wilson, D.; Valluzzi, R.; Kaplan, D. Conformational transitions in model silk peptides. *Biophysical journal* **2000,** *78* (5), 2690-2701.

(51) Teramoto, H.; Miyazawa, M. Molecular orientation behavior of silk sericin film as revealed by ATR infrared spectroscopy. *Biomacromolecules* **2005,** *6* (4), 2049-2057.

(52) Hu, X.; Kaplan, D.; Cebe, P. Determining beta-sheet crystallinity in fibrous proteins by thermal analysis and infrared spectroscopy. *Macromolecules* **2006,** *39* (18), 6161-6170.

(53) Chan, N. J.-A.; Gu, D.; Tan, S.; Fu, Q.; Pattison, T. G.; O'Connor, A. J.; Qiao, G. G. Spider-silk inspired polymeric networks by harnessing the mechanical potential of β-sheets through network guided assembly. *Nature communications* **2020,** *11* (1), 1-14.

(54) Keten, S.; Xu, Z.; Ihle, B.; Buehler, M. J. Nanoconfinement controls stiffness, strength and mechanical toughness of β-sheet crystals in silk. *Nature materials* **2010,** *9* (4), 359-367.

(55) Cho, S. Y.; Yun, Y. S.; Lee, S.; Jang, D.; Park, K.-Y.; Kim, J. K.; Kim, B. H.; Kang, K.; Kaplan, D. L.; Jin, H.-J. Carbonization of a stable β-sheet-rich silk protein into a pseudographitic pyroprotein. *Nature communications* **2015,** *6* (1), 1-7.

(56) Fu, C.; Porter, D.; Chen, X.; Vollrath, F.; Shao, Z. Understanding the mechanical properties of Antheraea pernyi silk—from primary structure to condensed structure of the protein. *Advanced Functional Materials* **2011,** *21* (4), 729-737.

(57) Li, M.; Tao, W.; Kuga, S.; Nishiyama, Y. Controlling molecular conformation of regenerated wild silk fibroin by aqueous ethanol treatment. *Polymers for Advanced Technologies* **2003,** *14* (10), 694-698.

(58) Teuschl, A. H.; Neutsch, L.; Monforte, X.; Rünzler, D.; van Griensven, M.; Gabor, F.; Redl, H. Enhanced cell adhesion on silk fibroin via lectin surface modification. *Acta biomaterialia* **2014,** *10* (6), 2506-2517.

(59) Leal-Egaña, A.; Scheibel, T. Interactions of cells with silk surfaces. *Journal of Materials Chemistry* **2012,** *22* (29), 14330-14336, DOI: 10.1039/C2JM31174G.

(60) Parekh, N.; Hushye, C.; Warunkar, S.; Sen Gupta, S.; Nisal, A. In vitro study of novel microparticle based silk fibroin scaffold with osteoblast-like cells for load-bearing osteo-regenerative applications. *RSC Advances* **2017,** *7* (43), 26551-26558, DOI: 10.1039/C7RA03288A.

(61) Guillaume, O.; Park, J.; Monforte, X.; Gruber-Blum, S.; Redl, H.; Petter-Puchner, A.; Teuschl, A. Fabrication of silk mesh with enhanced cytocompatibility: preliminary in vitro investigation toward cell-based therapy for hernia repair. *Journal of Materials Science: Materials in Medicine* **2016,** *27* (2), 37.

(62) Nisal, A.; Sayyad, R.; Dhavale, P.; Khude, B.; Deshpande, R.; Mapare, V.; Shukla, S.; Venugopalan, P. Silk fibroin micro-particle scaffolds with superior compression modulus and slow bioresorption for effective bone regeneration. *Scientific reports* **2018,** *8* (1), 1-10.

(63) Kang, Z.; Wang, Y.; Xu, J.; Song, G.; Ding, M.; Zhao, H.; Wang, J. An RGD-containing peptide derived from wild silkworm silk fibroin promotes cell adhesion and spreading. *Polymers* **2018,** *10* (11), 1193.

(64) Silva, S. S.; Kundu, B.; Lu, S.; Reis, R. L.; Kundu, S. C. Chinese oak tasar silkworm antheraea pernyi silk proteins: Current strategies and future perspectives for biomedical applications. *Macromolecular bioscience* **2019,** *19* (3), 1800252.

(65) Yanagihara, K.; Miki, M.; Ogawa, A.; Sasaki, M.; Yamada, H.; Terada, S. Effects of sericin on promoting proliferation and inhibiting apoptosis of mammalian cells. In *Animal Cell Technology: Basic & Applied Aspects*; Springer: 2008; pp 31-36.

(66) Luo, Y.; Wang, T. Pharmaceutical and Cosmetic Applications of Protein By-Products. In *Protein Byproducts*; Elsevier: 2016; pp 147-160.

(67) Ahmad, T.; McGrath, S.; Sirafim, C.; do Amaral, R. J.; Soong, S.-L.; Sitram, R.; Santarella, F.; Kearney, C. J. Development of wound healing scaffolds with precisely-triggered sequential release of therapeutic nanoparticles. *Biomaterials science* **2020**.

(68) Lanzalaco, S.; Del Valle, L. J.; Turon, P.; Weis, C.; Estrany, F.; Alemán, C.; Armelin, E. Polypropylene mesh for hernia repair with controllable cell adhesion/de-adhesion properties. *Journal of Materials Chemistry B* **2020,** *8* (5), 1049-1059.

(69) Zhang, W.; Li, Y.; Jiang, D.; Xie, S.; Zeng, M.; Chen, J.; Chen, L.; Ouyang, H.; Zou, X. Promotion of hernia repair with high-strength, flexible, and bioresorbable silk fibroin mesh in a large abdominal hernia model. *ACS Biomaterials Science & Engineering* **2017,** *4* (6), 2067-2080.

(70) Robinson, T.; Clarke, J.; Schoen, J.; Walsh, M. Major mesh-related complications following hernia repair. *Surgical Endoscopy and Other Interventional Techniques* **2005,** *19* (12), 1556-1560.

(71) Hawn, M. T.; Gray, S. H.; Snyder, C. W.; Graham, L. A.; Finan, K. R.; Vick, C. C. Predictors of mesh explantation after incisional hernia repair. *The American journal of surgery* **2011,** *202* (1), 28-33.

(72) Blatnik, J.; Jin, J.; Rosen, M. Abdominal hernia repair with bridging acellular dermal matrix—an expensive hernia sac. *The American journal of surgery* **2008,** *196* (1), 47-50.

(73) Melke, J.; Midha, S.; Ghosh, S.; Ito, K.; Hofmann, S. Silk fibroin as biomaterial for bone tissue engineering. *Acta biomaterialia* **2016,** *31*, 1-16.

(74) Fernández-García, L.; Marí-Buyé, N.; Barios, J. A.; Madurga, R.; Elices, M.; Pérez-Rigueiro, J.; Ramos, M.; Guinea, G. V.; González-Nieto, D. Safety and tolerability of silk fibroin hydrogels implanted into the mouse brain. *Acta biomaterialia* **2016,** *45*, 262-275.

(75) Zhang, W.; Chen, J.; Backman, L. J.; Malm, A. D.; Danielson, P. Surface topography and mechanical strain promote keratocyte phenotype and extracellular matrix formation in a biomimetic 3D corneal model. *Advanced healthcare materials* **2017,** *6* (5), 1601238.

(76) Mehrotra, S.; Chouhan, D.; Konwarh, R.; Kumar, M.; Jadi, P. K.; Mandal, B. B. Comprehensive review on silk at nanoscale for regenerative medicine and allied applications. *ACS Biomaterials Science & Engineering* **2019,** *5* (5), 2054-2078.

(77) Aramwit, P.; Kanokpanont, S.; De-Eknamkul, W.; Srichana, T. Monitoring of inflammatory mediators induced by silk sericin. *Journal of bioscience and bioengineering* **2009,** *107* (5), 556-561.

(78) Chandorkar, Y.; Basu, B. The foreign body response demystified. *ACS Biomaterials Science & Engineering* **2018,** *5* (1), 19-44.

(79) Anderson, J. M.; Rodriguez, A.; Chang, D. T. In *Foreign body reaction to biomaterials*, Seminars in immunology, Elsevier: 2008; pp 86-100.

(80) Sheikh, Z.; Brooks, P. J.; Barzilay, O.; Fine, N.; Glogauer, M. Macrophages, foreign body giant cells and their response to implantable biomaterials. *Materials* **2015,** *8* (9), 5671-5701.